PHYSICAL REVIEW A VOLUME 18, NUMBER 1 JULY 1978

Photoion angular distributions in dissociative photoionization of H_2 at 304 Å

J. L. Dehmer
Argonne National Laboratory, Argonne, Illinois 60439

Dan Dill
Department of Chemistry, Boston University, Boston, Massachusetts 02215

(Received 25 August 1977)

Photoionization of H_2 by 304-Å radiation can produce the $2p\sigma_u$, $2p\pi_u$, and $2s\sigma_g$ repulsive states of $H_2{}^+$. The angular distributions of energetic (> 2 eV) protons from these states have been measured relative to the incident unpolarized light beam using a rotatable hemispherical electrostatic analyzer. Axial-recoil conditions apply in this situation, so that the photofragment angular distribution would be $\sin^2\theta$ for pure $\Sigma\rightarrow\Sigma$ electronic transitions and $1+\cos^2\theta$ for pure $\Sigma\rightarrow\Pi$ electronic transitions. However, unlike photodissociation processes forming neutral products, the present process also involves the ejection of photoelectrons with alternative symmetries, each associated with one of the above characteristic photoion angular distributions. Consequently, measurement of the net photoion angular distribution in dissociative photoionization yields the branching ratio between the alternative (degenerate) channels available to the photoelectron. This type of information cannot be deduced by observing the photoelectron itself. The present results indicate that the formation of the $2p\sigma_u$ state $H_2{}^+$ at 304 Å is accompanied by ejection of photoelectrons with significant *d*-wave character.

I. INTRODUCTION

The measurement of angular distributions and kinetic energies of photodissociation products yields, respectively, information on the symmetry and internal energy of the dissociating parent state(s). This can be a uniquely powerful spectroscopic tool, particularly in regions of the photoabsorption spectrum dominated by diffuse bands which are characteristic of repulsive final states. Moreover, such measurements can provide dynamical information on the photoexcitation process, such as branching ratios and dissociation lifetimes. There is significant literature on the theoretical (see, e.g., Refs. 1–4) and experimental (see, e.g., Refs. 1, 4–6) aspects of this facet of molecular photodissociation; however, it is generally confined to the spectral range below the ionization potential.

In *dissociative photoionization,* a new wrinkle emerges: When a molecular ion is produced in a repulsive state by photoionization, the process also involves the ejection of photoelectrons, which generally have available to them degenerate ionization channels of more than one symmetry type. Since the photoion angular distribution yields symmetry information about the total final state (molecular ion plus photoelectron), this complicates the determination of the symmetry of the repulsive ionic state alone. On the other hand, when the repulsive state is known, this affords us the rare opportunity to directly measure the branching ratio for the alternative, degenerate ionization channels. This branching ratio cannot be obtained from the electron-energy spectrum owing to degeneracy; and the photoelectron angular distribution yields an implicit function of both the branching ratio and the relative phases of the alternative ionization channels from which the branching ratio cannot be isolated without further information. Once the branching-ratio information is obtained from the photoion angular distribution, however, it can be combined with the photoelectron angular distribution data to help unravel the information contained in the photoelectron asymmetry parameter. Under favorable conditions, described in Sec. II, the combination of photoion and photoelectron angular distributions can lead to a full determination of the dipole amplitudes and relative phases of the ionization channels, thus completely specifying all of the dynamical parameters of the photoionization process.

In this paper we present photoion angular distributions for dissociative photoionization of H_2 by 304-Å radiation. Under these conditions, the $2p\sigma_u$, $2p\pi_u$, and $2s\sigma_g$ repulsive states of H_2^+ are produced and decay under axial-recoil conditions owing to the large kinetic energies (>2 eV) of the fragments. Of these three states, particular attention is focused on the formation of the $2p\sigma_u$, which is clearly resolved in the photoion spectrum. In this case, we report the branching ratio for the σ_g and π_g photoelectron channels which are allowed by dipole-selection rules. The large contribution of π_g symmetry to the total photoelectron current implies significant *d*-wave ($l=2$) participation in the 304-Å photoionization of H_2. The $2p\pi_u$ and $2s\sigma_g$ ionic states are not completely resolved so that only the relative probability of $\Sigma\rightarrow\Sigma$ and $\Sigma\rightarrow\Pi$ transitions can be deduced.

II. THEORETICAL FRAMEWORK

Here we derive the general expression for the photoion angular distribution in dissociative photoionization of a homonuclear diatomic molecule in a $^1\Sigma$ state under axial-recoil conditions. To avoid obscuring the simple conclusions with theoretical detail, we indicate the three major results at the outset. (i) The main result is contained in Eq. (7). Here the net photoion asymmetry parameter is expressed in terms of the partial transition strengths for the dipole-allowed $\Sigma \to \Sigma, \Pi$ transitions. (ii) This result is then transformed into Eq. (11) which is used in the analysis of the present experimental data. Using Eq. (11), the measured photoion angular distributions yield the branching ratios of the $\Sigma \to \Sigma, \Pi$ photoionization transitions. This is translated into relative strengths of alternative photoelectron channels in Sec. IV. (iii) Finally, we note here the connection with photodissociation leading to a neutral final state. In this case, no photoelectron is ejected which can carry off alternative values of angular momentum, so that a single final-state symmetry results. Using Eq. (7), it is clear that $\beta = 2$ for $\Sigma \to \Sigma$ transitions and $\beta = -1$ for $\Sigma \to \Pi$ transitions, respectively. This in in agreement with the results of Zare in Ref. 1, to which the reader is referred for a detailed discussion of dissociation-product angular distribution in the absence of photoionization.

The following analysis is based on the so-called axial-recoil approximation,[1] which applies when the photofragments dissociate with a kinetic energy much larger than the rotational spacing. Under these circumstances, the observation direction of the photoion can be equated to the orientation of the internuclear axis at the time of photoionization This direction is specified by the set

$$\hat{R}_\gamma \equiv \{\alpha_\gamma, \beta_\gamma, \gamma_\gamma\} \tag{1}$$

of Euler angles of the rotations that carry the molecular-coordinate frame into the laboratory-coordinate frame, the latter defined by either the propagation direction or electric vector of the light. The cylindrical symmetry of the electric-dipole interaction renders the photoion (or photoelectron) angular distribution independent of γ_γ, which we set at $\gamma_\gamma = 0$. Similarly, the cylindrical symmetry of the molecule eliminates any dynamical dependence on α_γ (which we set at $\alpha_\gamma = 0$) although this is not generally true for molecules of arbitrary symmetry. Hence, dipole excitation of diatomic molecules depends dynamically only on the single angle β_γ.

The photoionization cross section $d\sigma/d\hat{R}_\gamma\, d\hat{k}_e$, differential in both $\hat{R}_\gamma$ and the photoelectron wave vector $\hat{k}_e$, is given by Dill in Eq. (15) of Ref. 7. By integration over the (unobserved) electron direction, one obtains the photofragment angular distribution in the axial-recoil approximation,

$$\begin{aligned}\frac{d\sigma}{d\hat{R}_\gamma} = 4\pi^2 \alpha h\nu (-1)^{m_p} & \times \sum_{l m m_\gamma m'_\gamma} (-1)^{m_\gamma} D^{(-)\Gamma_0 *}_{l m m'_\gamma} D^{(-)\Gamma_0}_{l m m_\gamma} \\ & \times \sum_{K_\gamma} \langle 1 m_\gamma, 1 - m'_\gamma | K_\gamma M_\gamma \rangle \\ & \times \langle 1 m_p, 1 - m_p | K_\gamma 0 \rangle D^{K_\gamma}_{M_\gamma 0}(\hat{R}_\gamma) .\end{aligned} \tag{2}$$

The zero index on the rotation-matrix element $D^{K_\gamma}_{M_\gamma 0}(\hat{R}_\gamma)$ reflects the dynamical independence of the result with respect to γ_γ. The quantum number m_p specifies light polarization and the laboratory z axis: $m_p = 0$ denotes linear polarization along z, and $m_p = \pm 1$ denotes left- and right-circular polarization about z. Photoionization dynamics determine the (molecule-frame) amplitudes

$$D^{(-)\Gamma_0}_{l m m_\gamma} = \left(\frac{4\pi}{3}\right)^{1/2} \int d\vec{r}\, \Psi^{(-)*}_{l m}(k_e, \vec{r}) r Y_{1 m_\gamma}(\hat{r}) \overline{\Psi}_{\Gamma_0}(\vec{r}) \tag{3}$$

for an electric dipole transition from the initial state $\overline{\Psi}_{\Gamma_0}(\vec{r})$ to the ingoing-wave-normalized continuum wave $\Psi^{(-)}_{l m}(k_e, \vec{r})$ represented in the molecule-fixed frame. The key features of Eq. (2) are the following: First, there is no interference between ionization amplitudes [Eq. (3)] with alternative orbital momenta l and projection m on the molecular axis, in contrast with the photoelectron angular distribution. Second, the maximum harmonic dependence is second order ($K_\gamma \leq 2$), so that the photofragment angular distribution can be relatively easily characterized experimentally, even for targets of general symmetry.

Further simplifications arise in the present case because the target is cylindrically symmetric and in a $\Gamma_0 = \Sigma$ initial state, and because the exciting radiation from a resonance lamp has natural polarization. The first of these conditions results in the simplification

$$m_\gamma = m'_\gamma = m , \tag{4}$$

so that only terms with $M_\gamma = 0$ occur in (2), reflecting the independence of the result with respect to α_γ mentioned earlier. The natural polarization can be treated in the usual way as an incoherent superposition of the two linear polarizations, which we derive first. Setting $m_p = 0$ in Eq. (2), corresponding to linear polarization, further restricts K_γ to be even, resulting in the only possible values $K_\gamma = 0, 2$. Combining these results, averaging over degenerate initial states, and explicitly evaluating the rotation-matrix elements and the Wigner coefficients, we obtain (see Ref. 8 for more detailed treatment)

$$\frac{d\sigma}{d\Omega_m}=\frac{\sigma}{4\pi}\,[1+\beta_m P_2(\cos\theta_m)]\,, \tag{5}$$

$$\sigma=\tfrac{4}{3}\,\pi^2\alpha h\nu(D_\Sigma^2+2D_\Pi^2)\,, \tag{6}$$

$$\beta_m=2(D_\Sigma^2-D_\Pi^2)/(D_\Sigma^2+2D_\Pi^2)\,, \tag{7}$$

where the subscript *m* denotes molecular fragment (to distinguish from *e* for electron) and we have introduced the symbols

$$D_\Sigma^2\equiv\sum_l\,|D_{l00}^{(-)\Sigma}|^2, \tag{8}$$

$$D_\Pi^2\equiv\sum_l|\,D_{l\pm1\pm1}^{(-)\Sigma}|^2 \tag{9}$$

for the total $\Sigma\rightarrow\Sigma$ and $\Sigma\rightarrow\Pi$ ionization strengths. Note that we have also replaced the second Euler angle β_γ by the more conventional angle θ_m of the molecular-fragment direction relative to the electric vector of the light, and $\hat{R}_\gamma$ by the solid angle Ω_m. This casts Eq. (5) in the form most familiar in photoelectron angular distribution studies. The asymmetry-parameter expression (7) predicts the intuitively expected results that, for linearly polarized light, pure $\Sigma\rightarrow\Sigma$ ionization will lead to a $\cos^2\theta_m$ distribution ($\beta=2$) and pure $\Sigma\rightarrow\Pi$ ionization will lead to a $\sin^2\theta_m$ distribution ($\beta=-1$).

Transformation to natural polarization gives

$$\frac{d\sigma}{d\Omega'_m}=\frac{\sigma}{4\pi}\left(1-\frac{\beta_m}{2}\,P_2(\cos\theta'_m)\right), \tag{10}$$

where Ω'_m and θ'_m refer now to the propagation axis of the light. Under unpolarized excitation conditions, therefore, pure $\Sigma\rightarrow\Sigma$ ionization yields a $\sin^2\theta'_m$ distribution and $\Sigma\rightarrow\Pi$ ionization a $1+\cos^2\theta'_m$ distribution. In the present case, however, a mixture of $\Sigma\rightarrow\Sigma$ and $\Sigma\rightarrow\Pi$ transitions are allowed so that the net photoion angular distribution, as reflected in the value of β_m, gives the relative strength of the two types of transition:

$$\frac{\sigma(\Sigma\rightarrow\Sigma)}{\sigma(\Sigma\rightarrow\Pi)}=\frac{D_\Sigma^2}{2D_\Pi^2}=\frac{1+\beta_m}{4-2\beta_m}\,. \tag{11}$$

Comparison of these results with those for photoelectron angular distributions emphasizes the complementarity of the two types of measurements. The photoelectron differential cross section for natural polarization is

$$\frac{d\sigma}{d\Omega'_e}=\frac{\sigma}{4\pi}\left(1-\frac{\beta_e}{2}\,P_2(\cos\theta'_e)\right), \tag{12}$$

where the subscript *e* denotes electron. The asymmetry parameter depends on the ionization channels contributing to a particular process and on the orbital momentum composition of photoelectric amplitude in each of these channels. The key element in β_e is that, since the angular distribution of photoelectrons is being measured, amplitudes corresponding to different orbital momenta superpose *coherently* to give interference terms both within and between alternative ionization channels. Consider, for example, ionization to the $2s\sigma_g$ state of H_2^+. Including $l=1$ (p) and $l=3$ (f) asymptotic orbital momenta only, and using the general expression for molecular asymmetry parameters, Eqs. (10)–(12) in Ref. 9 (see also Ref. 10 for explicit formulas), we obtain

$$\begin{aligned}\beta_e={}&[2/D_{p\sigma}^2+D_{f\sigma}^2+2D_{p\pi}^2+2D_{f\pi}^2)]\\&\times\{\tfrac{1}{5}\,[2D_{p\sigma}^2+7D_{p\pi}^2+6|D_{p\sigma}||D_{p\pi}|\cos\phi_{p\sigma p\pi}]+\tfrac{1}{15}\,[4D_{f\sigma}^2+9D_{f\pi}^2+2\sqrt{6}\,|D_{f\sigma}||D_{f\pi}|\cos\phi_{f\sigma f\pi}]\\&-\tfrac{1}{7}\sqrt{\tfrac{2}{5}}\,[|D_{f\sigma}||D_{p\sigma}|\cos\phi_{p\sigma f\sigma}-12|D_{f\pi}||D_{p\pi}|\cos\phi_{p\pi f\pi}]+\tfrac{3}{7}\sqrt{\tfrac{2}{5}}\,[4|D_{f\pi}||D_{p\sigma}|\cos\phi_{p\sigma f\pi}+\sqrt{6}\,|D_{f\sigma}||D_{p\pi}|\cos\phi_{p\pi f\sigma}]\}\,,\end{aligned} \tag{13}$$

where we have used the shorthand notation

$$D_{l\lambda}=D_{l,\pm\lambda,\pm\lambda}^{(-)\Sigma}\ \text{and}\ D_{l\lambda}^2=|D_{l\lambda}|^2,$$

and where

$$D_{l\lambda}=|D_{l\lambda}|e^{i\delta_{l\lambda}},$$

$$\phi_{l\lambda l'\lambda'}\equiv(\sigma_l-\sigma_{l'})+(\delta_{l\lambda}-\delta_{l'\lambda'})\,, \tag{14}$$

$$\sigma_l\equiv\arg\Gamma(l+1-iZ/k)\,,$$

where the $\delta_{l\lambda}$ are phase shifts relative to the Coulomb phase σ_l. The first two square brackets in the numerator of (13) represent the separate contributions of pure *p* and *f* waves and show the interference between alternative λ channels. The third bracket expresses the interference of alternative *l* values in the same λ channel, and the fourth the interference of alternative *l* values in different λ channels. In general, all three types of interferences will exist in molecular photoionization. Moreover, as more *l*'s are necessary to accurately describe the final-state wave function at larger *r*, the number of terms in Eq. (13) will grow rapidly. This can render the nature of β_e for molecular photoionization very complicated. Clearly, the photoion angular distribution, in which all these interference terms vanish, is much more easily interpreted and is therefore a parameter of great significance to the study of molecular photoionization. The most desirable case arises, e.g., at low energy or for relatively spherical targets, when only the lead orbital momenta contribute significantly to Eq. (13). Under these circumstances, the measurements of σ, β_m, and β_e combine to yield the sum, ratio, and relative phases of the ionization amplitudes, thus providing a complete characterization of the electronic part of the dissociative photoionization process.

III. EXPERIMENT

The rotatable hemispherical electrostatic analyzer used in these measurements is shown schematically in Fig. 1. Although usually used for electron detection, it was a simple matter to convert to a proton-detection mode by switching the power-supply polarities. The unpolarized 304-Å radiation was produced by a helium dc discharge in a hollow-cathode lamp. The present lamp is similar to that described earlier,[11] only now the cathode extends out of the rear of the lamp and is water cooled to enhance stability and increase the operating current. The gas pressure was typically 0.3 Torr and the current was ~1 A. The radiation was channeled into the ionization region by a 30.5-cm length of 2-mm-i.d. Pyrex capillary tubing (8). This channeling technique proved to be extremely efficient for light of this wavelength, enhancing the light intensity by more than two orders of magnitude while simultaneously eliminating the need for differential pumping of the lamp. Hydrogen gas effusing from the 1-mm channel in the molybdenum gas jet (10) crossed the light beam, and the resulting protons (and H_2^+) intercepted by the 1.5-mm entrance aperture (9) were energy analyzed and detected by a channeltron (7), having passed through the 1.5-mm exit aperture. The entrance and exit optics are simple in design, each consisting of a three-aperture "zoom" lens[12] (5), deflector plates (4), and Herzog lens[13] (3). The hemispheres were made by hydroforming a 4-mm copper plate against a hemispherical blank. A final machining step produced 2-in. mean-radius hemispherical surfaces which are accurate to 0.001 in. The resulting light weight of the analyzer resulted in ease of operation of the sapphire ball bearing (12) upon which the analyzer was mounted.

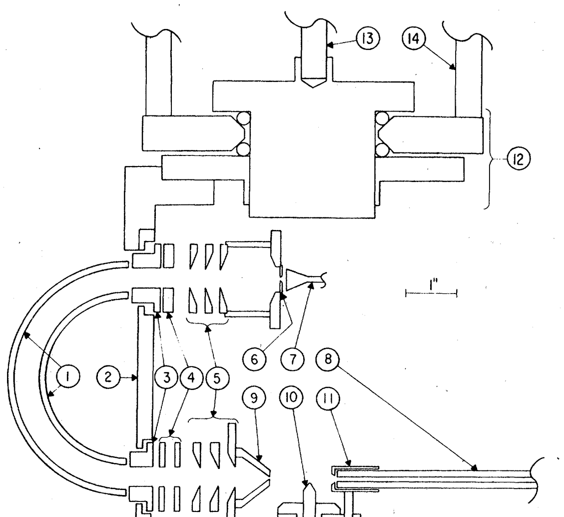

FIG. 1. Schematic diagram of the experimental apparatus. The main components are (1) concentric hemispheres, (2) mounting plate for hemispheres and entrance and exit lenses, (3) Herzog lenses, (4) deflector plates, (5) three-aperture "zoom" lenses, (6) exit aperture, (7) channeltron detector, (8) 2-mm-i.d. capillary tubing leading to the hollow-cathode discharge lamp (not shown), (9) entrance aperture, (10) effusive gas source, (11) shield and holder for capillary tube, (12) sapphire ball bearing, (13) drive shaft, and (14) mounting rods.

The analyzer was mounted in a vacuum chamber lined with two layers of high-permeability magnetic shielding, resulting in a residual magnetic field of <1 mG. Not shown in Fig. 1 is a cage of molybdenum gauze which was placed around the ionization region in order to eliminate electric fields from the region of space between the ionization region and the entrance aperture. The resulting environment enables high-resolution studies to be performed when smaller slits and low analysis energies are used, e.g., for 736-Å radiation on argon gas, 0.5-mm slit and 0.75-eV analysis energy has been observed to yield 0.006-eV full width at half-maximum (FWHM) resolution, including ~0.004 eV due to the width of the light beam.

In the present experiment, high sensitivity was called for due to the very small cross section for dissociative photoionization, ≪0.1 Mb for any given proton kinetic energy. Consequently, large apertures (1.5 mm) and a large (20 eV) kinetic energy in the dispersive element were used, resulting in a nominal resolution of 0.3 eV. Under the best conditions, a counting rate of ~5 $\sec^{-1}$ was achieved on the 5.5-eV H^+ peak. Spectra were recorded at several angles between $\theta = 20°$ and 90° and for maximum H^+ counts between 500 and 3000. The electron optics were set to focus at a single kinetic energy between 6 and 8 eV. Spot checks were run to check for effects of operating pressure (normally 5×10^{-5} Torr), focusing conditions, kinetic energy of analysis, and collision-zone geometry (i.e., jet-to-light-beam distance). None of these variations were found to significantly influence the results.

Under the present operating conditions, the distribution of target gas above the effusive gas jet is larger than the 2-mm diameter of the light beam, resulting in an elongated source of photoelectrons. This necessitated a geometric correction at each observation angle, which was determined by measuring the angular distribution of photoelectrons ejected from He by 304-Å radiation. The angle-dependent correction factor required to adjust the observed distribution to the correct one ($\beta = 2$) was then used to correct the photoion angular distribution. This process also corrects for any effect of finite angular resolution, which could be up to a factor of 2 larger than the ±2.2° calculated on the basis of a point source.

IV. RESULTS AND DISCUSSION

A. Spectroscopic background and interpretation

The potential-energy curves[14] for states of H_2 and H_2^+ important in our discussion of dissociative photoionization of H_2 at $\lambda = 304$ Å are given in Fig. 2. The shaded area denotes the Franck-Condon region of the $v = 0$ vibrational level of the ground state of H_2. Only transitions to those portions of the final-state potential-energy curves lying within this region will be appreciably populated in the photoionization process, with the excess energy being carried off by the photoelectron. Although ~2% of the transitions to the ground $1s\sigma_g$ ionic state of H_2^+ are dissociative,[15-18] the photofragment energy is very low and is not separated from the very intense H_2^+ peak in this work. The more energetic protons, which we are primarily concerned with, result from the three repulsive curves of H_2^+ lying above the $1s\sigma_g$ ground state. These states of the ion have $2p\sigma_u$, $2p\pi_u$, and $2s\sigma_g$ symmetries and are all the product of a two-electron excitation process. That is, one of the two $1s\sigma_g$ electrons in H_2 is ejected while the other remains behind but is excited into a higher electronic level of H_2^+. Table I contains a list of the dissociative photoionization channels associated with the three repulsive ionic curves listed in the second column. Based on the dipole-selection rules, which allow only $\Delta\lambda = 0, \pm 1$ and require a net parity change in the total wave function, the dipole-allowed photoelectron symmetries are listed in the third column, and the total channel symmetry is listed in the last column. Note that for channels 1–5 the parity change is undergone by the electron which remains behind while the ionized electron is ejected with the same parity it had in the initial state. Only in the production of the $2s\sigma_g$ ionic state is the "optical" electron (the one undergoing a parity change) the one being ionized. An analogous set of conditions has been studied in the case of photoionization of He.[19,20]

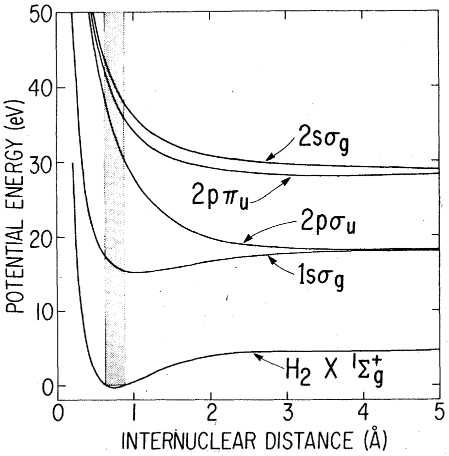

FIG. 2. Selected potential-energy curves (taken from Ref. 14) for states of H_2 and H_2^+ which participate in dissociative photoionization at $\lambda = 304$ Å. The shaded region represents the Franck-Condon region associated with the $H_2\ X\,^1\Sigma_g^+$ ($v = 0$) ground state.

In the analysis that follows, we use the theoretical framework presented in Sec. II to convert measured values of β_{H^+} into branching ratios between the dissociation channels given in Table I. We stress that this analysis depends only on an assignment of bands in the photoion spectrum to asymptotes of the repulsive H_2^+ curves in Fig. 2, and *not* upon the identification of the manifold of states, e.g., neutral Rydberg states converging to higher levels of H_2^+, which may act as intermediate states or otherwise participate in the dissociative photoionization process at small R. Moreover, the effects of such interaction mechanisms cannot be experimentally discerned at a single wavelength, even if that wavelength coincides with a Rydberg level which strongly influences the process. Rather, the qualitative identity of such a mechanism must rely on wavelength-dependent measurements which may reveal a strong energy variation of the branching ratios (and hence the β_{H^+}'s) in the vicinity of a known level of H_2. Of course, *ab initio* calculation of the observed branching ratios would require proper specification of all channels which significantly influence the process; but, as stated above, this is not a prerequisite for determining these same quantities from photoion angular distributions.

Information on the participation of autoionizing states in dissociative photoionization is sparse, even for H_2. Clear evidence has been reported at $\hbar\omega = 26.9$ eV by Strathdee and Browning[21]; but no similar evidence exists for $\hbar\omega = 40.8$ eV, although, in their study of photoion energy spectra at this

TABLE I. Dissociative photoionization channels for H_2 at $h\nu = 304$ Å.

Channel	Symmetry of H_2^+ ionic state	Dipole-allowed photoelectron symmetry	Total ionic core plus photoelectron channel symmetry
1	$2p\sigma_u$	σ_g	Σ_u
2	$2p\sigma_u$	π_g	Π_u
3	$2p\pi_u$	σ_g	Π_u
4	$2p\pi_u$	π_g	Σ_u
5	$2p\pi_u$	δ_g	Π_u
6	$2s\sigma_g$	σ_u	Σ_u
7	$2s\sigma_g$	π_u	Π_u

wavelength, Gardner and Samson[22] noted that "autoionization through neutral terms leading to the $2p\pi_u$ and $2s\sigma_g$ states of H_2^+ may be appreciably populated with 40.8-eV photons." Therefore, the distinct possibility for this type of mechanism exists, but cannot yet be established for the case studied here. The extensive studies[23] of dissociative ionization of H_2 by electron impact may also provide insight into the role of autoionizing states. However, the participation of the whole manifold of dipole-forbidden states and the undetermined excitation energy in each collision limits the utility of this avenue for the present purposes. Also, in recent theoretical work, possible autoionizing states of H_2 have been discussed in connection with dissociation phenomena, for example, by Botcher[24] and Hazi[25]; however, these states lie too low in the spectrum to significantly influence the processes studied here. Of these diverse studies, the one which bears most directly on the present work is that by Gardner and Samson,[22] who used a calibrated energy analyzer to obtain accurate H^+ intensity distributions in the range 0–12 eV. They found that the shape of their results at $\hbar\omega = 40.8$ eV was well accounted for by fitting to the Franck-Condon distribution for direct excitation of the $2p\sigma_u$, $2p\pi_u$, and $2s\sigma_g$ states of H_2^+. In fact, they found that the $2s\sigma_g$ state seemed to play a negligible role in the dissociative photoionization process at this wavelength. This general conclusion was also drawn in a related experiment by Wood *et al.*,[26] who used fast He^+ ions to ionize H_2. Although we need make no assumptions regarding the relative importance of direct or indirect mechanisms, we will investigate the consequences of assuming that dissociative photoionization of H_2 at $\hbar\omega = 40.8$ eV is dominated by direct transitions to the $2p\sigma_u$ and $2p\pi_u$ states of H_2^+.

Figure 3 contains representative photion kinetic energy spectra resulting from photoionization of H_2 by 304-Å radiation. The dependence of the spectra on the angle of observation relative to the incident, unpolarized light beam is seen qualitatively in the $\theta = 20°$, 90° spectra and will be discussed quantitatively below. The identification of the spectral features follows easily from the preceding discussion: The strong peak near zero kinetic energy is comprised mostly of ground-state H_2^+ ions plus a small (2%) admixture of H^+ ions from dissociation of the H_2^+ $1s\sigma_g$ ground state, as mentioned above. The doublet structure between 2 and 12 eV is two orders of magnitude weaker and represents the energetic protons from the three purely repulsive H_2^+ states immediately above the ground ionic state. The band centered at 5.5 eV is attributable to a superposition of ions from the $2p\pi_u$ and $2s\sigma_g$ states, but is probably predominantly from the $2p\pi_u$ state. The weaker band

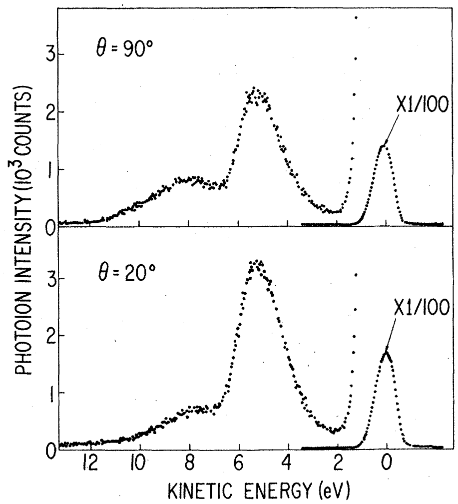

FIG. 3. Photoion kinetic-energy spectra for photoionization of H_2 ($\lambda = 304$ Å) at two observation angles ($\theta = 20°$, 90°) relative to the incident unpolarized light beam. The large peak near zero kinetic energy is comprised mostly of $H_2^+ 1s\sigma_g$ ground-state ions, which have a thermal-energy distribution. Note that these two spectra are uncorrected for the spectrometer transmission function or differences in source geometry for the two observation angles (see text).

at 8 eV is known to correspond to protons from dissociation of the $2p\sigma_u$ state. The present data are not corrected for the transmission of the spectrometer, which is higher for slower particles. This accounts for the difference in appearance between the present data and that of Gardner and Samson,[22] which shows the 5.5- and 8-eV peaks are comparable in intensity. Note that the lack of calibration in no way interferes with the quantitative angular dependence of this spectrum.

B. Photoion angular distributions

The two spectra in Fig. 3 permit the qualitative observation that the 5.5-eV band is peaked forward, along the direction of the light, while the 8-eV band is slightly larger perpendicular to the light direction. Hence, one can expect the asymmetry parameter β_{H^+} [Eq. (10)] will be negative for the 5.5-eV peak and positive for the 8-eV peak. This qualitative observation is put on a quantitative basis in the lower part of Fig. 4, where the β_{H^+} value was determined at evenly spaced energy intervals between 3 and 9 eV.[27] The spread in the data, due to weak signal and long counting times, necessitated the large error bars which were drawn, conservatively, to cover the range of variation of all runs. Despite the large uncertainty, a dramatic variation in the angular distribution of energetic protons from this process is observed. At 9-eV kinetic energy, where protons are produced only from the $2p\sigma_u$ state, $\beta_{H^+} \cong 0.86$. As the influence of the 5.5-eV peak increases at ~8-eV kinetic energy, the β_{H^+} value begins to plummet toward its low value of $\beta \cong -0.3$ near 6 eV. The data exhibit a very gradual net rise between 6 and 3 eV which we are not sure is significant. On the one hand, the rise is no larger than the error bars, but, on the other hand, it repeats as an internal trend in each set of data. If it's real it might indicate a variation in the mixture of the dominant $2p\pi_u$ and weaker $2s\sigma_g$ states in the unresolved 5.5-eV band. Otherwise it could be due to interference from the H_2^+ peak or imperfections in the focusing of very-low-energy particles. We are unable to resolve this issue here, and focus, instead, on the gross trends observable in Fig. 4.

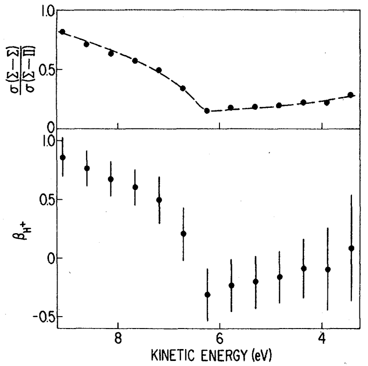

FIG. 4. Asymmetry parameter and resulting relative cross sections for $\Sigma \rightarrow \Sigma$ and $\Sigma \rightarrow \Pi$ type transitions for 3–9-eV protons produced by dissociative photoionization of H_2 at $\lambda = 304$ Å.

C. Branching ratios for degenerate photoionization channels

The net ratio of cross sections for $\Sigma \rightarrow \Sigma$ and $\Sigma \rightarrow \Pi$ transitions are given in the upper part of Fig. 4. This curve has been deduced from the β_{H^+} curve using Eq. (11), and the error bars have been omitted. The limit of $\sigma(\Sigma \rightarrow \Sigma)/\sigma(\Sigma \rightarrow \Pi) \cong 0.82$ at 9 eV can be taken as representative of dissociative photoionization via the H_2^+ $2p\sigma_u$ state. This indicates

$$\sigma(\Sigma \rightarrow \Sigma)/\sigma(\Sigma \rightarrow \Pi) = \sigma_1/\sigma_2 = 0.82$$

(where the subscripts denote channel numbers in Table I) so that production of π_g photoelectrons is ~20% more probable than production of σ_g photoelectrons in connection with protons formed with ~9-eV kinetic energy. Since π_g and σ_g wave functions have $l = 2$ and $l = 0$ lead terms, respectively, (in a spherical harmonic representation) this observation implies that d waves contribute strongly to photoionization of H_2 at $\lambda = 304$ Å. The importance of high-l partial waves to molecular photoionization has been recently emphasized[9] in photoionization of heavier first-row diatomic molecules. We reemphasize that this partitioning of excitation probability between degenerate ionization channels would not be possible by measurements on the photoelectrons themselves. This new information provides a very detailed check of future theoretical calculations of dissociative photoionization of hydrogen, and, moreover, could be combined with photoelectron angular distributions to help unravel the relative phases of the alternative photoionization channels.

The information deduced from the branching ratio in the vicinity of the 5.5-eV peak is complicated by alternative $\Sigma \rightarrow \Sigma$ and $\Sigma \rightarrow \Pi$ channels. If we take 0.15 as representative of the branching ratio in this region of the spectrum, we find that

$$\frac{\sigma(\Sigma \rightarrow \Sigma)}{\sigma(\Sigma \rightarrow \Pi)} = \frac{\sigma_4 + \sigma_6}{\sigma_3 + \sigma_5 + \sigma_7} = 0.15\,,$$

where, once again, the subscripts denote channels given in Table I. If it is true that the 5.5-eV peak is dominated by the H_2^+ $2p\pi_u$ state, then the information we learn is simpler:

$$\frac{\sigma(\Sigma \rightarrow \Sigma)}{\sigma(\Sigma \rightarrow \Pi)} = \frac{\sigma_4}{\sigma_3 + \sigma_5} = 0.15\,.$$

This indicates that the sum of photoionization via the σ_g and δ_g channels is much stronger than that proceeding via the π_g photoionization channel. The net result probably reflects the dominance of the $l=0$ component of the σ_g wave function over the higher angular momentum species comprising channel 4. This differs from the result for the $2p\sigma_u$ state because the photoelectron energy is decreased for the higher H_2^+ ionic curves, which would be accompanied by a reduced d-wave contribution to the photoionization process.

A final remark concerns an assumption implicit in our theoretical analysis. The use of Eq. (2) [or, more generally, Eq. (15) of Ref. 7 from which it is derived] assumes that the cross sections for production of alternative repulsive states of H_2^+ sum incoherently when only the proton is detected as in the present experiment. The incoherence is clear in the case of the $2p\sigma_u$ state of H_2^+ since the recoiling protons from this state are isolated by energy analysis. Less obvious is the case of the $2p\pi_u$ and $2s\sigma_g$ states owing to the degeneracy of the asymptotic energies for protons coming from these states. Nevertheless, the cross sections for production of these states also sum incoherently under the present conditions. This results from the opposite parities of the continuum electrons corresponding to these alternative dissociation channels. Hence, all interference terms, which are proportional to the product of electronic functions of opposite parity, vanish when integrated over the (unobserved) electronic coordinates. In circumstances where the electronic parities are the same, interference may arise between channels dissociating to the same asymptote, thus requiring an extension of the formulation presented here.

ACKNOWLEDGMENTS

One of us (J. L. D.) would like to thank several co-workers for their innovative suggestions and advice which significantly contributed to the instrument used in these measurements. These include members of the Building 203 branch of Argonne's Central Shops, D. Spence, W. T. Jivery, P. M. Dehmer, and W. A. Chupka. We also wish to thank Dr. J. Durup for his helpful comments which led to the remark at the end of Sec. IV C concerning possible coherence effects. This work was performed in part under the auspices of the U. S. Department of Energy. One of us (D. D.) would like to thank the Alfred P. Sloan Foundation for financial support.

---

[1] R. N. Zare, Mol. Photochem. 4, 1 (1972).
[2] Sze-cheng Yang and R. Bersohn, J. Chem. Phys. 61, 4400 (1974).
[3] R. C. Ormerod, W. R. Anderson, and T. L. Rose, J. Chem. Phys. 62, 127 (1975).
[4] J. H. Ling and K. R. Wilson, J. Chem. Phys. 65, 881 (1976).
[5] R. C. Ormerod, T. R. Powers, and T. L. Rose, J. Chem. Phys. 60, 5109 (1974).
[6] E. J. Stone, G. M. Lawrence, and C. E. Fairchild, J. Chem. Phys. 65, 5083 (1976).
[7] Dan Dill, J. Chem. Phys. 65, 1130 (1976).
[8] Scott Wallace and Dan Dill, Phys. Rev. B 17, 1692 (1978).
[9] J. L. Dehmer and Dan Dill, J. Chem. Phys. 65, 5327 (1976).
[10] J. Siegel, D. Dill, and J. L. Dehmer (unpublished).
[11] J. L. Dehmer and J. Berkowitz, Phys. Rev. A 10, 484 (1974).
[12] F. H. Read, J. Phys. E 3, 127 (1970).
[13] R. Herzog, Z. Phys. 97, 596 (1935).
[14] T. E. Sharp, At. Data 2, 119 (1971).
[15] G. H. Dunn, J. Chem. Phys. 44, 2592 (1966).
[16] J. Fryar and R. Browning, Planet. Space Sci. 21, 709 (1973).
[17] C. Backx, G. R. Wight, and M. J. van der Wiel, J. Phys. B 9, 315 (1976), and references therein.
[18] A. L. Ford and K. Kirby Docken, J. Chem. Phys. 62, 4955 (1975).
[19] M. O. Krause and F. Wuilleumier, J. Phys. B 5, L143 (1972).
[20] V. L. Jacobs and P. G. Burke, J. Phys. B 5, L67 (1972).
[21] S. Strathdee and R. Browning, J. Phys. B 9, L505 (1976).
[22] J. L. Gardner and J. A. R. Samson, Phys. Rev. A 12, 1404 (1975).
[23] For recent work on this subject, which contains an extensive bibliography of earlier work, see R. J. van Brunt, Phys. Rev. A 16, 1309 (1977).
[24] C. Bottcher, J. Phys. B 7, L352 (1974).
[25] A. U. Hazi, J. Phys. B 8, L262 (1975).
[26] R. M. Wood, A. K. Edwards, and M. F. Steuer, Phys. Rev. A 15, 1433 (1977).
[27] Since we were unable to reliably deconvolute the 5.5- and 8-eV proton peaks, and since the composition of the 5.5-eV peak could vary as a function of proton kinetic energy, we felt it was necessary to report β_{H^+} as a function of proton energy rather than to try to report a single β_{H^+} value for each of the two bands. This was done in three steps. First, a smooth curve was hand-drawn through each spectrum and the photoion intensities at thirteen points (those for which β_{H^+} values are reported in Fig. 4) were recorded. Second, the data at each angle was multiplied by the geometric factor discussed in Sec. III, which corrects for the elongated source shape. Third, the corrected intensities at each proton energy and observation angle were converted to a value of β_{H^+} by comparing $\theta \neq 90°$ intensity with the two bracketing $\theta = 90°$ measurements. (The $\theta = 90°$ measurements were interspersed between each $\theta \neq 90°$ scan to check the stability of the appartatus, e.g., the lamp stability.)